RESEARCH ARTICLE

ADVANCED MATERIALS INTERFACES Open Access

www.advmatinterfaces.de

Ferrofluid-Based Bioink for 3D Printed Skeletal Muscle Tissues with Enhanced Force and Magnetic Response

Judith Fuentes, Maria Guix, Zoran M. Cenev, Anna C. Bakenecker, Noelia Ruiz-González, Grégory Beaune, Jaakko V.I. Timonen, Samuel Sanchez,* and Veronika Magdanz**

3D printing has emerged as a transformative technology in several manufacturing processes, being of particular interest in biomedical research for allowing the creation of 3D structures that mimic native tissues. The process of tissue 3D printing entails the construction of functional, 3D tissue structures. In this article, the integration of ferrofluid consisting of iron oxide nanoparticles into muscle cell-laden bioink is presented to obtain a 3D printed magnetically responsive muscle tissue, i.e., the ferromuscle. Using extrusion-based methods, the seamless integration of biocompatible ferrofluids are achieved to cell-laden hydrogels. The resulting ferromuscle tissue exhibits improved tissue differentiation demonstrated by the increased force output upon electrical stimulation compared to muscle tissue prepared without ferrofluid. Moreover, the magnetic component originating from the iron oxide nanoparticles allows magnetic guidance, as well as good cytocompatibility and biodegradability in cell culture. These findings offer a new versatile fabrication approach to integrate magnetic components into living constructs, with potential applications as bioactuators and for future integration in smart, functional muscle implants.

1. Introduction

Biofabrication involves the generation of biologically functional products with high degree of complexity, characterized by structural organization, utilizing biomaterials such as bioactive molecules, living cells, or multicellular systems.[1] 3D bioprinting is an established biofabrication method enabling the generation of 3D constructs with preprogrammed geometries by the layer-by-layer deposition of bioinks to form functional tissue structures.[2] Bioinks play a crucial role as an integral component in the bioprinting process, undergoing cross-linking or stabilization either during or immediately after the printing. One of the main advantages of 3D bioprinting is its ability to generate mechanically stable and complex structures with a higher level of automation when compared with traditional techniques such as mold casting. This is particularly relevant for skeletal muscle tissue engineering and regeneration, where 3D scaffolds must exhibit a specific structural organization, and the bioink must create a myogenic environment, meaning it should provide the biological and physiological conditions necessary for proper muscle cell maturation to obtain fully functional tissue.[3] The choice of bioink composition is contingent upon the specific application, such as the type of cells involved, and the

J. Fuentes, M. Guix, A. C. Bakenecker, N. Ruiz-González, S. Sanchez, V. Magdanz
Institute for Bioengineering of Catalonia (IBEC)
Barcelona Institute of Science and Technology (BIST)
Baldiri-Reixac 10–12, Barcelona 08028, Spain
E-mail: maria.guix@ub.edu; ssanchez@ibecbarcelona.eu; veronika.magdanz@uwaterloo.ca

M. Guix
Department of Materials Science and Physical Chemistry
Institute of Theoretical and Computational Chemistry
University of Barcelona
Barcelona, Catalonia 08028, Spain

Z. M. Cenev, G. Beaune, J. V. Timonen
Department of Applied Physics
School of Science
Aalto University
Puumiehenkuja 2, Espoo 02150, Finland

Z. M. Cenev
Department of Mechanical and Production Engineering
Aarhus University
Katrinebjergvej 89F-5128, Aarhus 8200, Denmark

A. C. Bakenecker
Medical Engineering
Technical University of Darmstadt
Merckstr. 25, 64283 Darmstadt, Germany

S. Sanchez
Institució Catalana de Recerca i Estudis Avançats (ICREA)
Passeig de Lluís Companys 23, Barcelona 08010, Spain

V. Magdanz
Department of Systems Design Engineering
Waterloo Institute for Nanotechnology
University of Waterloo
200 University Ave W, Waterloo, ON N2L 3G1, Canada

The ORCID identification number(s) for the author(s) of this article can be found under https://doi.org/10.1002/admi.202400824

DOI: 10.1002/admi.202400824

utilized bioprinter.[4] For example, decellularized extracellular matrix -derived bioinks have gained significant interest due to its ability to provide a native-like microenvironment that supports cell adhesion, proliferation, and differentiation.[5] Similarly, several organic and inorganic materials have been integrated in bioinks, aiming to develop composite scaffolds with advanced capabilities.[6] Such composite materials can promote biological processes to achieve improved tissue differentiation and repair by i) enhancing conductivity when stimulated with electrical,[7] magnetic fields,[8] ii) or by chemical cues,[9] and/or iii) providing mechanical cues for cell organization. In fact, the integration of magnetic components into hydrogels for tissue engineering has been widely studied, and their influence on cell growth and alignment for regenerative medicine strategies has been explored.[10] In tissue engineering, magnetic nanoparticles have found interest for the fabrication of organized tissues driving their appropriate functionalization.[11] For applications in regenerative medicine, magnetic nanoparticles have shown to enhance stem cell differentiation in several areas such as bone, muscle and connective tissue. The implementation and clinical translation of superparamagnetic nanoparticles in regenerative medicine is promising, as these particles have been FDA-approved for several diagnostic and therapeutic applications such as contract agents for magnetic resonance imaging, hyperthermia cancer treatment and treatment of iron deficiency.[12]

One of the key approaches to obtain controlled cell alignment is the implementation of anisotropic distribution of the magnetic component. In that regard, the magnetic elements can be integrated either by directly including them in the hydrogel to obtain tunable responses to magnetic stimulation,[13] or in the substrate where skeletal muscle cells will be later seeded, like the magneto-active microfiber mesh obtained via melt electrowriting (MEW)[14] or rolled-up structures fabricated using 4D printing.[15] However, none of these approaches have attempted the fabrication of magnetic bioink, i.e., the direct printing of a cell-laden, magnetic ink into 3D tissue structures.

Magnetic hydrogels, so-called ferrogels, have also shown self-healing effects and potential utilization as tissue scaffolds and drug delivery systems.[16,17] Biphasic ferrogels containing an iron oxide gradient have shown a positive effect on muscle regeneration in mice, offering new strategies for drug release and in situ muscle stimulation.[18–20] One of the challenges in 3D bioprinting for tissue regeneration and implant placement is integration into the host tissue to ensure proper function and connection to the surrounding target tissue. Further, control over the implant positioning and improved imaging capabilities by embedded contrast agents is a desirable feature of smart implants. All of these goals can be achieved by developing a magnetic, cell-laden bioink compatible with the printing process and cell differentiation, and offers improved tissue integration, imaging and positioning abilities by external magnetic fields.

Here, we present a magnetic bioink for the 3D printing of a ferromuscle, namely a fully functional magnetic muscle tissue consisting of mouse myoblasts mixed within a hydrogel blend of gelatin/fibrinogen and a water-based ferrofluid (i.e., citrated iron oxide nanoparticles). The ferromuscle tissue was fabricated using extrusion-based 3D printing, a versatile fabrication technique for advanced biomaterials. The biocompatibility of the ferrofluid was evaluated, observing also an enhanced force output for the ferromuscle when compared to control muscle tissues (non-magnetic tissues). Due to the presence of iron oxide nanoparticles, the ferromuscle can be magnetically actuated and navigated facilitating magnetic-based cell migration throughout tissues, while being fully degradable upon removal of protease inhibitors. We demonstrate the potential of our homogeneous ferrofluid-based bioink for the biofabrication of skeletal muscle tissues with advanced performance, of interest both for the development of relevant 3D models for medical applications and biohybrid actuators. Moreover, this bioink can be easily implemented in the regenerative medicine field, offering an innovative solution for improved tissue repair and growth by guiding cells into the host tissue through magnetic manipulation.

2. Results and Discussion

2.1. 3D Printing with Murine Skeletal Muscle Cells and Ferrofluid

Among different fabrication approaches for bioengineered muscle tissue, such as molding or electrospinning, extrusion-based 3D printing gained interest during the past years due to its versatility, biocompatibility and induction of polymer and cell alignment during the extrusion process.[21] Therefore, we used this fabrication technique for the development of magnetic skeletal muscle tissue prints (**Figure 1A**). To create the bioink, C2C12 mouse myoblasts were combined with a gelatin-fibrinogen-based hydrogel and ferrofluid obtaining a homogenous mixture. Gelatin was employed as a viscosity modulator, enabling the optimal mechanical properties required for extrusion printing. This bioink is then extruded in an 8-shape geometry around flexible Polydimethylsiloxane (PDMS) posts, as shown in Figure 1D. The bioink, containing C2C12 cells and 1% ferrofluid that presents a characteristic brownish color, attributed to the ferrofluid containing the superparamagnetic iron oxide particles. The color intensity varies according to its concentration (Figure 1B,C). After printing, the fibrinogen inside the bioink is enzymatically cross-linked with thrombin, inducing the formation of fibrin, which provides structural stability to the scaffold. Then, the 3D bioprinted tissue is immersed first in growth medium for 2 days, followed by at least 7 days in differentiation medium, cultured under sterile conditions in an incubator providing 5% carbon dioxide and 37 °C controlled environment. Thanks to the tension provided by the PDMS post system, the myoblasts differentiate into aligned multinucleated myotubes, forming a stretched and taut muscle construct (Figure 1D). The two posts in the construct provide tension and mechanical stability, facilitating muscle differentiation and the formation of aligned myotubes, crucial for proper force contraction, as demonstrated in Figure 1E,F. The myosin heavy chain II, a marker for muscle differentiation, is clearly visible in Figure 1E (green), indicating the full maturation of the C2C12 myoblasts into multinucleated myotubes. The bright dots in Figure 1F show the distribution of the iron oxide nanoparticles inside the muscle fiber.

To assess the impact of ferrofluid integration on the bioink printability, we characterized the rheological properties of the ferrogels and its stability once cells are added into the

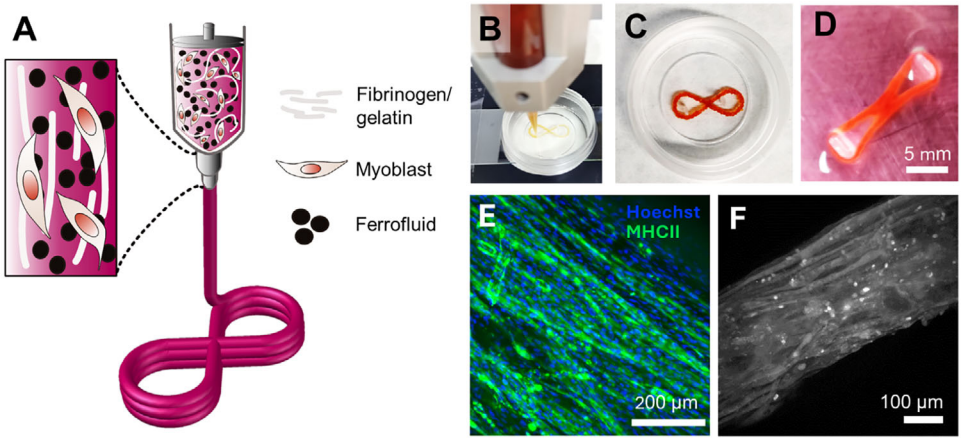

Figure 1. Biofabrication of ferromuscles by extrusion-based 3D bioprinting. A) Schematic of bioprinting of magnetic muscle tissue. Mouse myoblasts C2C12 are mixed with a hydrogel composed of 7% w/v gelatin, 4% w/v of fibrinogen and 1–5% ferrofluid, and then 3D printed by extrusion. Illustration not to scale. B) 3D printed ferromuslce containing C2C12 skeletal mouse muscle cells and 1% ferrofluid are printed in an 8-shape around previously prepared flexible PDMS posts. C) Photograph of the ferromuscle tissue containing C2C12 cells with 5% ferrofluid right after bioprinting. D) Ferromuscle stretched and differentiated after 6 days of culture. The 2-post system provides tension to support muscle differentiation. E) Immunofluorescence staining of Myosin Heavy Chain IIb (green) and cell nucleus (Hoechst, blue) showing the formation of aligned and multinucleated myotubes in ferromuscles. F) Confocal image of the 3D internal structure of a ferromuscle sample at inclination angle of 40° after 1 week of culture. Bright spots indicate the distribution of ferrofluid.

mixture (ferromuscle). The rheological assessment included control gels (gelatin/fibrinogen-based hydrogels without ferrofluid) and ferrogels (gelatin/fibrinogen-based hydrogels with ferrofluid) at different ferrofluid concentrations (e.g., 1%, 2.5%, and 5%) (**Figure 2**). Both control and ferrogels exhibit non-Newtonian behavior, as evidenced by the shear stress and viscosity curves (Figure 2A). By increasing the shear rate, a higher shear stress and reduced viscosity is observed. The viscosity reduction is attributed to the shear-thinning characteristics of these hydrogels, being a desirable property in extrusion-based 3D bioprinting. This behavior allows for the control of bioink viscosity, ensuring a homogeneous flow through the nozzle by adjusting pressure during printing. Comparing the control gel with various ferrogels reveals that the integration of ferrofluid, at a concentration from 1 – 5% ferrofluid, does not significantly impact the rheological properties of the bioink (Figure 2A). To fully conclude that the printability of ferrogels remains comparable to that of control gels, we characterized the geometry of the 3D bioprinted ferromuscle after printing and cross-linking processes. Top and side views of control muscle and ferromuscle (2.5% of ferrofluid concentration) printed with one, two, and three layers can be observed in Figure 2B. Additionally, Figure 2C,D shows the measured fiber width (measured from top view images) and fiber height (measured from side view images) of the prints, respectively. Regardless of the presence of ferrofluid in the bioink, the width and height of the bioprinted tissues increase with every subsequent bioprinted layer, both for post-bioprinting and post-cross-linking evaluation, demonstrating that the desired shape is preserved throughout the biofabrication process. Only the two-layer ferromuscle tissues showed slightly reduced width and height when compared to control tissues, which we correlated with a reduced gelation rate of the magnetic bioink. Despite these minor differences the printability of the magnetic bioink was not substantially affected by the integration of ferrofluid.

2.2. Magnetic Characterization of the Ferromuscle

The material properties of the ferrofluid solution, as well as its further characterization when integrated in 3D printed ferromuscle, were evaluated. The ferrofluid consists of superparamagnetic iron oxide nanoparticles with an average diameter of 10.3 ± 3.8 nm, as shown in the transmission electron microscopy (TEM) images (Figure S1a,b, Supporting Information). By using Vibrating Sample Magnetometry (VSM), we further characterized the magnetic response of all constituting materials (experimental details in Supporting Information). The non-magnetic 3D printed muscle tissue (control) presents a diamagnetic response, while the water-based ferrofluid containing citrated iron oxide nanoparticles exhibits a superparamagnetic response (Figure S1c, Supporting Information). Notably, the ferromuscle displays a very similar superparamagnetic response to the ferrofluid, with a maximum offset disparity of 36.1% observed at the 1T magnetic field strength data point. More specifically, the saturation magnetization for the ferromuscle is 2.96 A m^{-1}, while for the ferrofluid is 4.03 A m^{-1}. Based on the ferromuscle composition for the VSM evaluation (see Supporting Information), the mass fraction of magnetic nanoparticles in 1 mL of solid sample in the ferrogel is approximated to 1.9%. Therefore, it is reasonable to expect that the majority of the magnetic nanoparticles within the ferrofluid remain incorporated into the structure of the ferromuscle, while a small portion may be washed away during culture media exchange, justifying the offset disparity in the volume magnetization from the VSM measurements.

2.3. Degradation of the Ferromuscle Tissue

Usually in cell culture of 3D printed cell-laden structures, the addition of protease inhibitors such as aminocaproic acid (ACA) avoids the degradation of fibrinogen-based materials in the

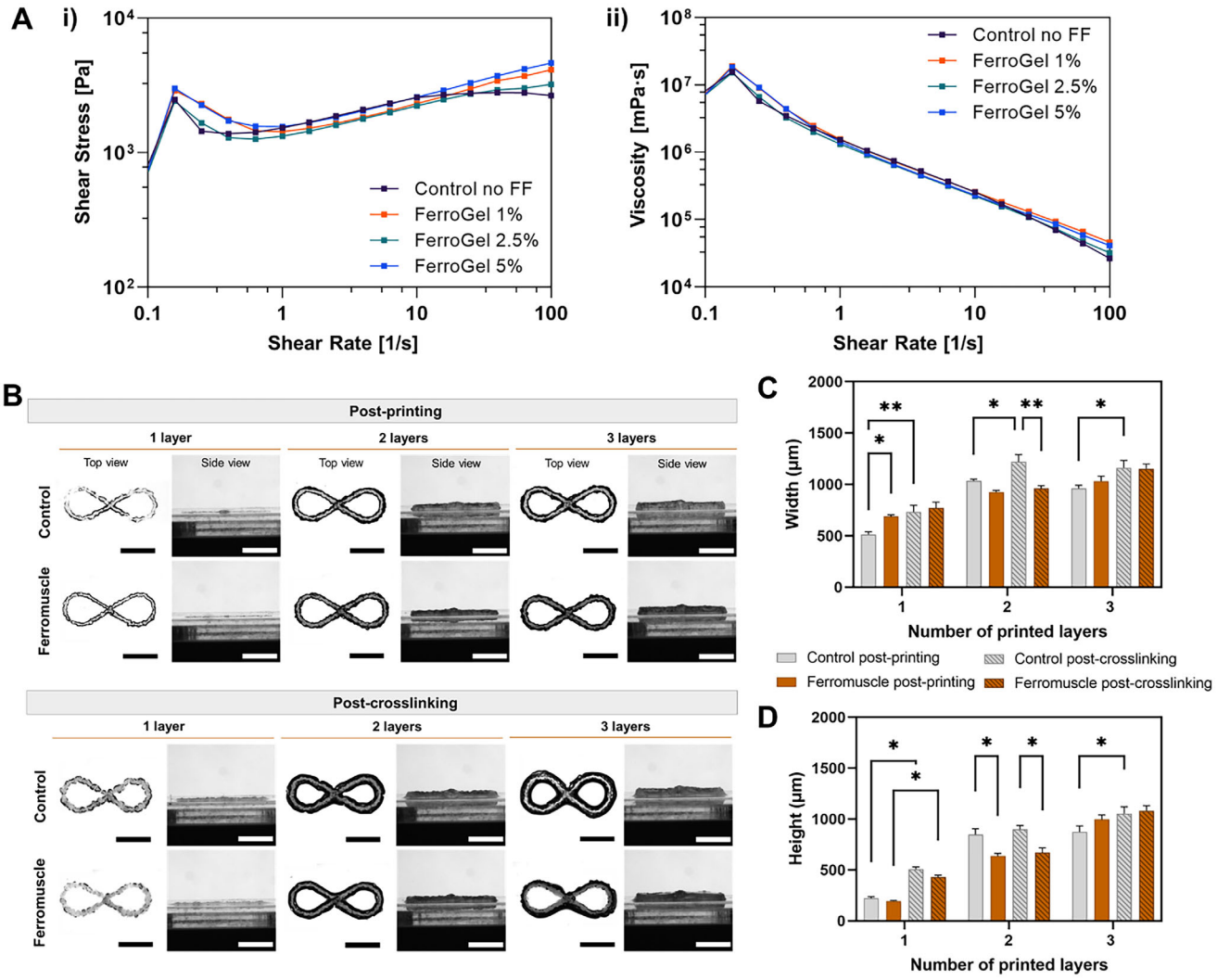

Figure 2. Printability evaluation of ferrofluid-based bioink. A) Rheological characterization of ferrogel containing different concentrations of ferrofluid: i) Flow curves and ii) viscosity curves. B) Top and side views (obtained with optical microscopy) of 1, 2, and 3 layers of control and ferromuscle tissues (2.5% ferrofluid) printed at 70 kPa of relative pressure, right after printing (top panel) and after bioink cross-linking with thrombin (bottom panel). Scale bars correspond to 5 mm. C) Width (i.e., fiber diameter, measured from top-view images) of the control and ferromuscles before and after cross-linking. D) Height (measured from side view images) of the control and ferromuscles before and after cross-linking. Images were taken from $N = 4$ independent repeats. All values are represented as mean ± standard error of the mean (SEM). $*p < 0.05$ (Two-way analysis of variance (ANOVA) followed by Turkey's multiple comparisons test).

resulting bioprinted structures.[22] To demonstrate the sustainability and degradability of the ferromuscle, we conducted degradation studies of the 3D printed ferromuscle samples (**Figure 3**). After full differentiation of the ferromuscle on day 9 of culture, the muscle tissues were cultured in differentiation media without ACA over 21 days. Figure 3A displays how the muscle tissue shrinks over time, observing only a few remains of cell-laden hydrogel and the post structures. After 14 days of culture without ACA, more than 70% of tissue is degraded in both control and ferromuscle samples. The level of degradation is slightly reduced in the ferromuscle containing 5% of ferrofluid, but for 1% and 2.5% similar to the control tissue. These ranges of ferrofluid also resulted in best force output, therefore, can be considered the optimum concentration of ferrofluid. Contrarily, the muscle tissues that were cultured in the differentiation medium with ACA maintained their structure over the 21 days of culture. These results demonstrate that the integration of ferrofluid does not significantly affect the degradability of the tissues over time. Nevertheless, it is important to mention that the diameter of the tissue changes over time naturally due to i) the dissolution of the uncross-linked gelatin and ii) due to the matrix remodeling by the skeletal muscle cells. The dissolution of gelatin, however, occurs progressively during the muscle maturation process. Gelatin provides biologically active moieties, such as hydrolyzed collagen, that enhance cell growth, migration, and proliferation[23] and therefore we hypothesize that these cell-matrix interactions help retain the gelatin within the construct for at least the time points of these experiments.

In our experiments, the nanoparticles from the degraded tissue were flushed out during the regular media change. In an in

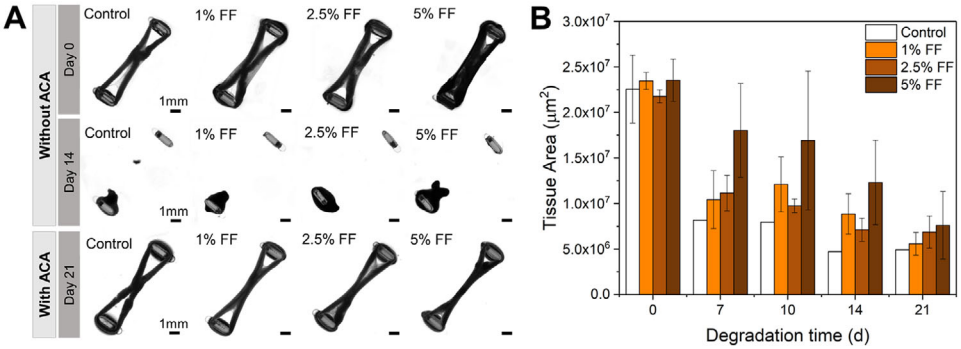

Figure 3. Degradation of the ferromuscle in cell culture. A) Brightfield images of ferromuscle samples with different concentrations of ferrofluid (0,1,2.5,5%) at day 0 and day 14 of cultivation in differentiation medium without protease inhibitor (ACA). B) Tissue area measured from images at different time points over degradation time of 21 days.

vivo setting, nanoparticles might degrade via several pathways, resorbed by the media, and the lymphatic system can clear particles of such small size (<11 nm).[11,24]

Prior to clinical studies, it will be important to explore their long-term intracellular fate and understand whether they behave as indissoluble units or can in fact be degraded by the cells over longer time periods. The primary concerns associated with a possible biodegradation would be the risk of a decreased magnetic response and the potential toxicity brought by the release of iron ions.[24]Possible biodegradation pathways include macrophage internalization in liver, spleen, kidney, and bone marrow, where the nanoparticles are subjected to a progressive acid-induced degradation. Released iron is then stored in ferritin protein.[11] However, due to the high degree of complexity, precise quantification of iron particle degradation is difficult.

2.4. Viability, Functionality, and Biological Characterization of the Ferromuscle

To evaluate if the integration of ferrofluid induces a cytotoxic effect on the muscle cells, viability tests were performed at day 3 and 6 after 3D bioprinting (**Figure** 4A,B). Slightly significant differences in cell viability were observed on day 3 between control (0% ferrofluid), 1%, 2.5%, and 5% ferrofluid with probability values of $p = 0.004$, 0.01, and 0.002, respectively. On day 6, these differences diminished and no significant differences in viability between control muscle and ferromuscle were observed, indicating that the ferrofluid integration into the bioink does not impair muscle cell viability. Noticeably, the samples containing 2.5% even showed a slightly increased viability compared to the control sample after six days of culture ($p = 0.009$).

We performed functionality tests to evaluate the force contraction of the ferromuscles on day 9, assuming full differentiation at this point. These muscle tissues were maintained on the two-post systems, which allowed the force measurements upon controlled electrical stimulation of the muscle. This method was conducted according to previous studies, that correlate the bending distance of the PDMS posts to the bending force of the muscle.[25] Euler-Bernoulli's beam bending equation was used to evaluate the tension that the tissue applied to the post during force contraction.

The muscle tissues were stimulated with a DC voltage of 15 V at a frequency of 1 Hz with 2 ms pulse width. The displacement of the PDMS posts were recorded and analyzed with a tailor-made python tracking script (Figure 2C). The control muscle tissue generates on average 27.7 ± 5.3 µN, while ferromuscle exerts an enhanced force output when increasing ferrofluid content from 1% to 2.5%, showing a contraction force of 65.8 ± 13.9 and 82.6 ± 14.6 µN, respectively, being a 160% and 250% force output in comparison with control tissues. At 5% ferrofluid content, the muscle force drops to a value similar to the control without any ferrofluid (23.3 ± 3.6 µN). These results demonstrate that a fully functional tissue is achieved when embedding murine skeletal muscle cells within the ferrofluid-based bioink, and the optimal ferrofluid concentration is 2.5%, suggesting that the addition of superparamagnetic nanoparticles leads to enhanced muscle differentiation

The positive effect of iron oxide nanomaterials on promoting cell alignment and myogenic differentiation in skeletal muscle tissue for in vivo skeletal muscle regeneration has been demonstrated by using anisotropic conductive, biodegradable hydrogels loaded with iron oxide-modified carbon nanotubes[13] as well as magnetic nanofibrous scaffolds composed of electrospun gelatin and polyurethane fibers embedded with iron oxide nanoparticles.[26] Such impact has also been observed among other nanomaterials, like gold nanoparticles, attributing this effect to the trigger myogenic differentiation in vitro.[27] Another example of the nanoparticles' positive effect are muscle-based biobots with improved force contraction and motion obtained by integrating boron nitride nanotubes (BNNTs) with piezoelectric properties into the cell-laden scaffold.[28] It has been hypothesized in many works that nanoparticles have a beneficial effect on cell differentiation. It is thought that metallic nanoparticles activate certain differentiation pathways, but the underlying mechanisms are still known.[29]

In line with these findings, we can hypothesize that the increased contraction force observed in the ferromuscle could be attributed to an improved differentiation of the muscle cells as a result of their interaction with the ferrofluid nanoparticles. In the majority of the reported studies, the benefits of integrating magnetic nanoparticles into scaffolds and composites come from the modulation of their alignment through magnetic fields, creating an anisotropic environment that promotes optimal

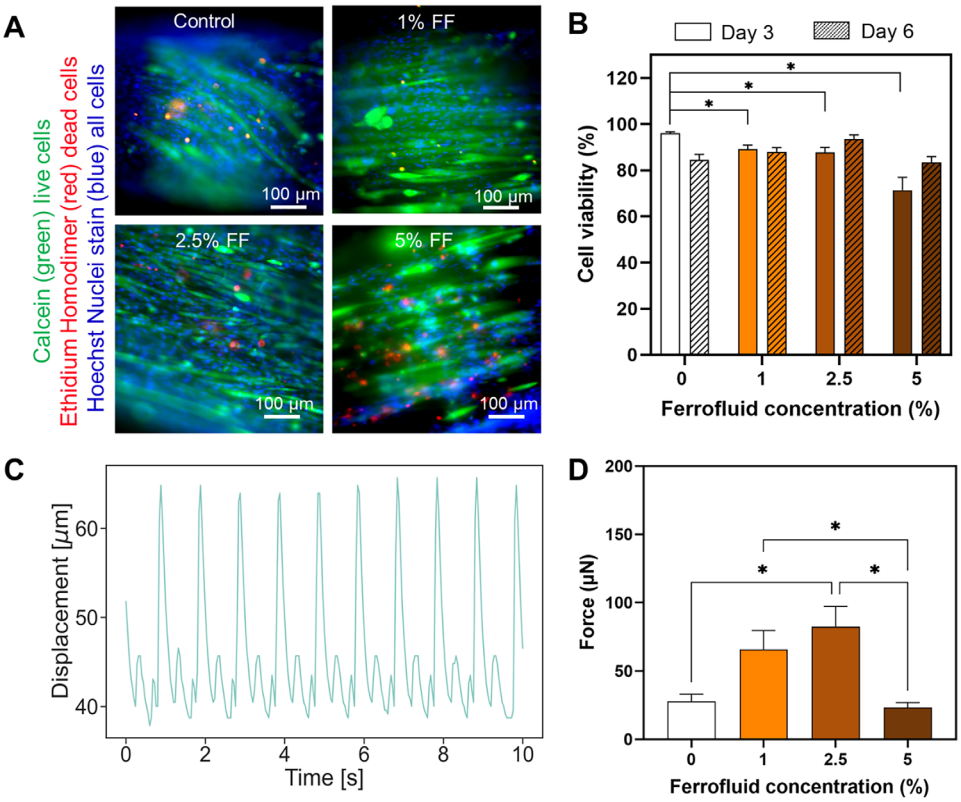

Figure 4. Ferromuscle viability and contraction force upon electric stimulation. A) Viability of muscle cells 3D bioprinted after 3 days in culture. Blue stains show cell nuclei (Hoechst), red cells are dead cells (Ethidium homodimer), green cells are live myocytes (calcein). Elongated myocytes demonstrate the start of muscle differentiation. B) Viability obtained from live/dead stains of bioprinted skeletal muscle cells on day 3 and day 6 show good cell compatibility of the ferrofluid. C) When electrical stimulation is applied, (1Hz, 15 V), the muscle tissue contracts periodically and results in the displacement of the flexible post over time. D) Average contraction forces generated by the differentiated ferromuscle versus the ferrofluid content.

differentiation of skeletal muscle cells.[13,30] In this study, however, no magnetic fields were applied during the 3D printing of the ferromuscle or the muscle differentiation process. Therefore, to better understand the underlying biological mechanisms responsible for the observed enhanced contraction force in ferromuscles, we investigated the effect of integrating ferrofluid in the skeletal muscle scaffold both at genetic and morphological levels. Real-time quantitative PCR (RT-qPCR) analysis was performed to evaluate and compare the differentiation process of ferromuscles containing 2.5% ferrofluid (the concentration that resulted in the strongest tissues) against control tissues. Since multinucleated myotubes arise from the differentiation of myoblasts into myocytes, followed by their fusion into myotubes, we assessed the expression of key marker genes involved in this process. These included MyoD (myoblast marker) and Myogenin (myocyte marker), along with maturation-related genes associated with Myosin Heavy Chain (MyHCI, MyHCIIa, and MyHCIIb), as shown in Figure S3 (Supporting Information). Overall, we observed common expression patterns,[25,31] including the downregulation of MyoD over time and the upregulation of myotube markers (MyHCI, MyHCIIa, and MyHCIIb). However, the downregulation of MyoD was statistically significant only in ferromuscles, while the upregulation of MyHC-related genes was statistically significant only in control tissues. In control tissues these findings suggest a more progressive differentiation of myoblast into myocytes and the subsequent fusion into myotubes, while ferromuscle do not follow the same pattern, especially in the early differentiation-related genes. In general, we observed lower expression levels of MyHC genes in ferromuscles compared to control tissues, with significant downregulation on day 9 for MyHCIIa and at day 4 for MyHCIIb. Interestingly, despite these changes, there were no significant differences in MyHCIIb and MyHCI expression between the samples at day 9 (the time point at which muscle contraction was evaluated), suggesting that the enhanced contraction force in ferromuscles may not be directly linked to the expression levels of these maturation-related genes; instead, we hypothesized that it may result from morphological and structural factors. Therefore, we further evaluated cell organization in control and ferromuscles at different time points through fluorescence imaging of F-actin (filamentous actin), one of the main components of the cell cytoskeleton. As shown in **Figure 5**A, on day 0 of differentiation (the day when growth media was switched to differentiation media, two days after 3D bioprinting), cells in control tissues were more randomly organized, while ferromuscle cells already started to show slight level of alignment. On day 4, multinucleated myotubes could be observed in both control and ferromuscle, although the ones in ferromuscle appeared more organized. By

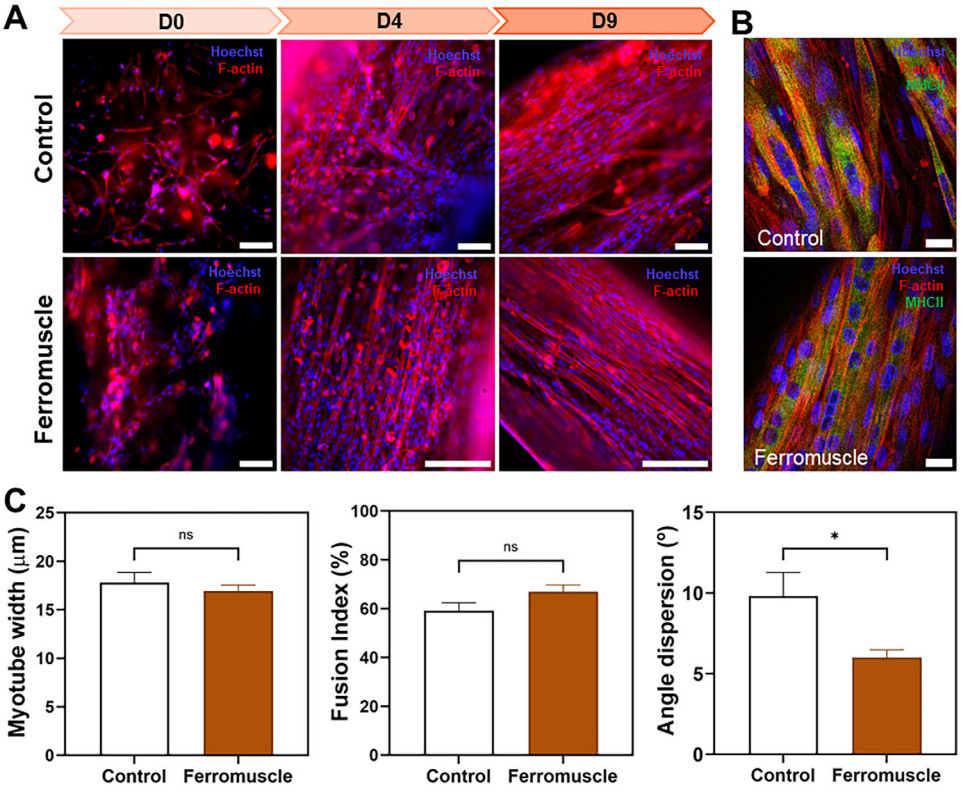

Figure 5. Evaluation of muscle cell differentiation into multinucleated myotubes in ferromuscle and control tissues. A) Fluorescence imaging of F-actin and nucleus (Hoechst) of control and ferromuscles at day 0, 4, and 9 of differentiation (scale bar = 200 μm). Please note that day 0 (D0) of differentiation refers to the day when the growth media was switched to differentiation media, which occurred two days after the 3D bioprinting of the tissues. B) Immunofluorescence staining of Myosin Heavy Chain IIb (MHCII), F-actin, and cell nucleus of control and Ferromuscles at day 9 of differentiation (scale bar = 20 μm). C) Graph displaying the values of myotube width (μm), fusion index (%), and angle dispersion (°) of myotubes (i.e., myotube directionality). Higher values of angle dispersion indicate less orientation and alignment of the muscle fibers. All values are represented as mean ± SEM. Statistical significance was assessed using an unpaired multiple t-test ($p < 0.05$ (*)).

day 9, fully matured myotubes were observed in both types of tissue.

To better assess the morphological changes of the mature myotube samples, we also evaluated the size, fusion index (percentage of myocytes that have fused to form multinucleated myotubes) and directionality, staining them with both for MyHCIIb and F-actin (Figure 5B,C). No significant differences in myotube size and fusion index were observed, suggesting that the efficiency of myoblast fusion during muscle maturation is similar in both control and ferromuscle tissues. Remarkably, we found a significant increase in the angle dispersion of myotubes in control tissues. Angle dispersion reflects the level of myotube directionality, where higher values indicate less orientation and lower level of alignment of the muscle fibers. Therefore, these results suggest that, although myotubes in ferromuscles exhibit similar characteristics in terms of size and fusion index, they are notably more aligned in comparison to those in control samples.

Based on these findings, we believe that the enhanced force contraction may result from better myotube organization, as it is well known that myotube alignment and directionality are essential for the generation or coordinated and efficient force.[32]

We also hypothesize that this improved alignment of myotubes is likely due to the combined effect of two factors: i) the integration of ferrofluid nanoparticles into the bioink, which may further enhance the cell alignment already promoted by the 3D bioprinting process, as it is known to induce the alignment of both cells and polymer networks during extrusion,[33] and ii) the mechanical tension provided by the flexible posts during culture, which could further contribute to the improved organization.

2.5. Magnetically Induced Migration of Bi-Layered Muscle and Ferromuscle Composite

As a proof-of-concept, we evaluated whether the magnetically induced migration of magnetic nanoparticles could improve tissue-to-tissue attachment and cell migration into neighboring tissues under the influence of a magnetic gradient field, aiming to recreate the process of ferromuscle transplantation for regeneration purposes. The exposure of magnetic nanoparticles inside the tissue to a static external permanent magnet induces the attraction of the particles toward the magnet and thus possible particle and cell migration in that direction. A magnetic field gradient is formed by being strongest on the magnet surface and

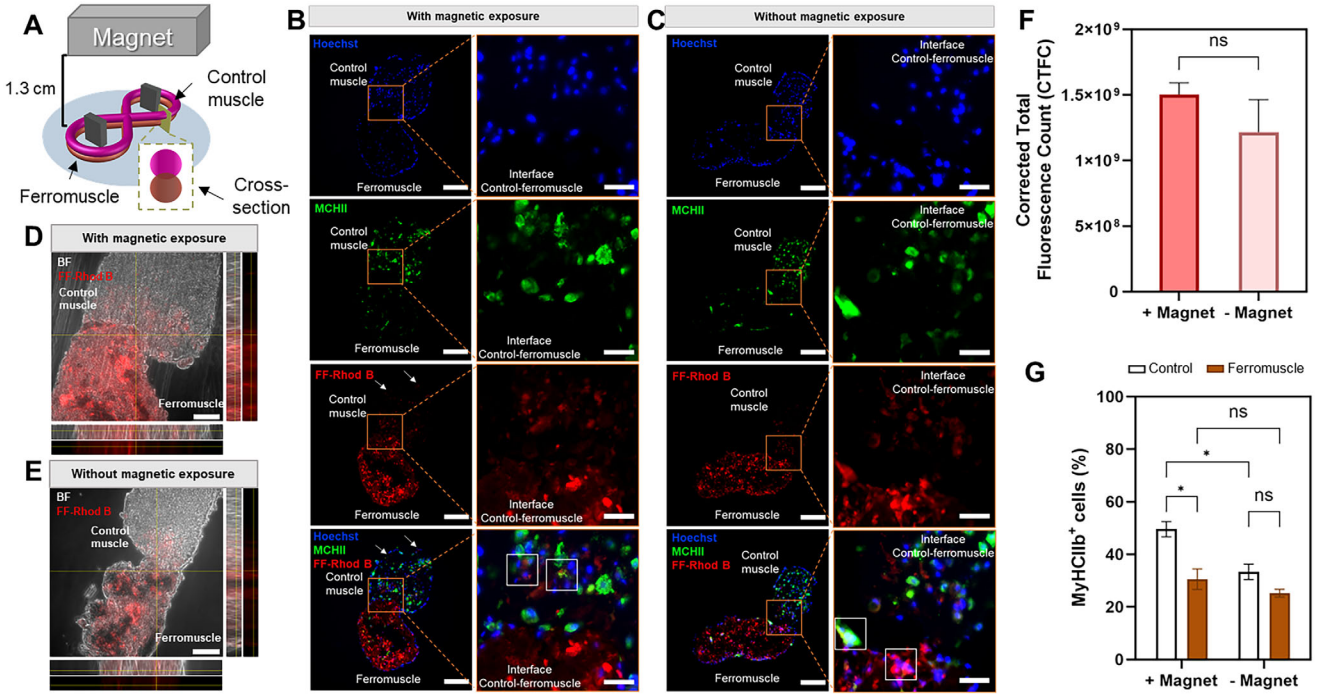

Figure 6. Influence of magnetic field on cell migration through muscle tissues and ferromuscle. A) Schematic representation of the co-culture of control muscle (top) and ferromuscle (bottom) for 7 days under magnetic stimulation with permanent magnet to induce the migration of ferrofluid nanoparticles from the ferromuscle to the control muscle. B,C) Immunofluorescence staining of cross sections from co-cultured control and ferromuscles exposed to magnetic field (B) and not exposed to magnetic field (C), showing the penetration of Rhodamine B-labeled ferrofluid and cell migration from the ferromuscle into the control muscle (scale bar = 200 µm). White arrows indicate the presence of fluorescent ferrofluid Nanoparticles in the control tissue. Orange framed areas correspond to the interface between the two muscle tissues (scale bars = 50 µm). White squares indicate the areas were a co-localization of Hoechst, MyHCII, and Rhodamine-labeled ferrofluid was observed. D,E) Orthogonal projections of images from C) and D), respectively (scale bar = 100 µm). F) Quantification of the ferrofluid penetration by the corrected total cell fluorescence (CTFC = Integrated fluorescence intensity – (Area x mean fluorescent of background) of the FF-Rhod B signal obtained in the area of control tissues. All values are represented as mean ± SEM. Statistical significance was assessed using an unpaired multiple t-test ($p < 0.05$(*)). G) Quantification of the percentage of MyHCIIb-positive cells observed in control and ferromuscle tissues of both magnetized and non-magnetized samples. All values are represented as mean ± SEM. Statistical significance was assessed using a two-way analysis of variance (ANOVA) followed by Tukey's multiple comparisons test ($p < 0.05$(*)).

diminishes with distance, following an inverse power law. This effect could aid the integration of the printed tissue into a target tissue location. To replicate an implantation scenario, we cultured a 3D bioprinted control muscle (containing no ferrofluid) directly on top of ferromuscle (containing 2.5% of ferrofluid), as illustrated in **Figure** 6A. Both control and ferromuscles were bioprinted separately in a two-post system and left in growth medium for 2 days and in differentiation media for 2 days. Afterward, control tissue was transferred to the petri dish onto the ferromuscles. Subsequently, the samples were left for 7 days i) under no external influence, and ii) under influence of a static magnetic field gradient originating from a neodymium permanent magnet placed on top of the petri dish. The ferrofluid concentration within the ferromuscle tissue was 2.5% of iron oxide nanoparticles conjugated with Rhodamine B. In this experiment, iron oxide nanoparticles were stained to visualize ferrofluid migration.

Immunofluorescence images from the cross sections of the co-cultured muscles tissues (Figure 6B,C) show more concentration of muscle cells in the control tissues in comparison with the ferromuscle, indicated by the higher presence of stained nucleus and MHCIIb-positive cells, regardless of magnetic exposure. In contrast, more fluorescent ferrofluid nanoparticles (FF-Rodh B nanoparticles) were observed in the ferromuscles and in the interface of the two muscle tissues. Overlapping signals from Hoechst and/or MyHCIIb, and Rhodamine-stained ferrofluid were observed, suggesting potential internalization of the magnetic nanoparticles within the skeletal muscle cells, as highlighted in the white square in the merged images (Figure 6B,C). Although ferrofluid nanoparticles were found in the top part of the control muscles in both the magnetically and in the non-exposed samples (Figure 6B), in the case of the control samples which was magnetically exposed sample, slightly higher concentration of fluorescent nanoparticles was observed. In the images from orthogonal projections we can observe an improved penetration of the ferrofluid to deeper areas of the control tissue, presenting a higher signal in the top part of the Y axis projection (Figure 6D) when compared to the non-magnetically exposed samples (Figure 6E). We also quantified the migration of the ferrofluid by measuring the fluorescence intensity of the Rhodamine-labeled ferrofluid particles that migrated into the adjacent control muscle tissues. Our results showed a higher fluorescence signal in the magnetized samples, but it should be noted that this increase was not statistically significant compared to the

non-magnetized samples (Figure 6F). Remarkably, when quantifying the percentage of MyHCIIb-positive cells in both control and ferromuscle tissues, with and without magnetic exposure, we observed a significantly higher presence of MyHCIIb-positive cells in control tissues compared to ferromuscles in samples with magnetic exposure (Figure 6G). In contrast, no significant differences were observed between the two tissues in non-magnetized samples, suggesting that magnetic exposure notably enhanced cell migration from the ferromuscle tissue to the adjacent control tissue.

Finally, regarding the level of tissue-to-tissue attachment, we observed that the interface area between control and ferromuscle tissues was larger in the sample exposed to magnetic field, suggesting that such conditions improve the interactions between tissues. These results demonstrate the potential of our magnetic bioink for fabricating 3D tissues for regenerative applications, as well as the promising opportunity for using magnetic nanoparticles in future targeted guidance driven by magnetic fields.[34]

2.6. Motion of a Ferromuscle Tissue under Influence of Non-Uniform Magnetic Field from a Permanent Magnet

Last, we demonstrate the magnetic response of a ferromuscle released from the two-post system by using a static external magnetic field gradient originating from a permanent magnet placed beside the dish (Figure S4A and Video S1, Supporting Information). The magnetic response demonstration was performed on ferromuscle containing 2.5% ferrofluid on day 9. The ferromuscle was showing spontaneous contractions, inherent to mature muscle tissues.[35] These spontaneous contractions were observed in our experiments when the muscle structure was still attached to the PDMS posts, e.g. during contraction analysis, but also immediately after release from the posts, as can be seen in Video S1 (Supporting Information). This type of "twitching" muscle motion can be seen in the smaller peaks of contractions in Figure 4C.

Such spontaneous contractions are also visible in Video S2 (Supporting Information), showing the fluorescent real-time video of the cell nuclei (stained blue) moving during the muscle contraction. Figure S4A (Supporting Information) demonstrates the linear trajectory of the ferromuscle toward the permanent magnet located on the opposite side of the petri dish. The motion is not constant (Figure S4C, Supporting Information), as the ferromuscle was not electrically stimulated and the actuation came from spontaneous contractions, which are not controllable. An average speed of 1.88 mm s^{-1} was obtained, demonstrating for the first time magnetic response of functional muscle tissue by motion within a magnetic field gradient.[31,36] However, the motion of the ferromuscle is not fully derived from the contractions but from the overlayed gradient of the magnetic field imposed by the permanent magnet, hence the muscle speed does not correlate to the speed of the muscle action. Magnetic control under electrical stimulation is demonstrated in Video S3 (Supporting Information), which also illustrates that the non-magnetic control tissue on the bottom left of the video is stimulated in the same way and shows contractions, but does not respond to the external magnetic field and therefore does not show translational movement. Such control could be of great interest both in tissue regeneration for advanced manipulation purposes and in the field of biohybrid actuators, where external programmable guidance is essential to develop smart robotic systems.

3. Conclusion

In this study, we developed a magnetic bioink composed of C2C12 mouse myoblasts, a gelatin- and fibrinogen-based hydrogel, and a water-based ferrofluid solution. Notably, the iron oxide nanoparticles were homogeneously distributed in the bioink formulation and rheological properties of the resulting magnetic bioink were the same as the control bioink. The ferromuscle was successfully differentiated into myotubes and magnetic properties were maintained. Indeed, the bioink showed optimal printability conditions even for cell-laden bioinks, as demonstrated for the 3D bioprinting of magnetic muscle tissue (ferromuscle). Our results show that integrating 1% and 2.5% of ferrofluid in the myoblasts muscle tissue increases muscle contraction force by more than 160% and 250%, respectively; while further increase of ferrofluid amount to the muscle (e.g., 5%) did not show a significant change in the muscle force output. Genetic and morphological studies suggest that ferrofluid integration may have a minimal impact on the regulation of maturation-related genes but could enhance cell reorganization and myotube alignment, which are crucial for effective muscle contraction. Further, we present a fabrication protocol that demonstrates satisfying cytocompatibility throughout the process and can be expected to be implemented with other cell types, of special interest in the regenerative medicine field. The muscle coculture experiments were performed to elucidate the interaction between cultured ferromuscles and control muscles and aimed to recreate a process of tissue integration. In case of major muscle loss due to injury or other tissue loss, the ferromuscle construct are envisioned to be a novel alternative that provides enhanced muscle force, differentiation and support of implant integration in the future. In an implantation scenario a continuous magnet application for prolonged periods of time, for instance by utilizing an adhesive magnetic patch, could lead to the here indicated enhancements in cell migration and muscle force output. This has been proposed as an approach in previous works[18] for the continuous magnetic stimulation of a non-cellular ferrogel placed on top of a muscle injury. Adhesive magnetic patches are commercially available and currently used for their potential health benefits in supporting pain relief and healing and could easily be adapted for this purpose. However, further research should be done in order to evaluate if the integration of ferrofluid into engineered tissues will indeed improve muscle performance in vivo. Additionally, the magnetic response of the ferromuscle has been demonstrated by motion and directionality studies. Achieving refined magnetic control in biohybrid constructs is one of the main challenges in the development of biohybrid actuators, where control and automation are pivotal to their design. Overall, the bioprinting approach hereby presented offers additional control over the resulting engineered tissue, as well being of great interest in the field of tissue engineering and implant technology. This approach is envisioned to be impactful for smart tissue repair, not only in muscle tissues but also in other types of tissue (e.g., skin, cartilage, or bone), and for the development of biohybrid actuators with advanced control capabilities.

4. Experimental Section

Ferrofluid Preparation: Synthesis of Citrate Maghemite (Fe_2O_3) Nanoparticles in Distilled Water: Fe_2O_3 nanoparticles were synthesized using the Massart process,[37] as the procedure was previously described.[38] Briefly, magnetite nanoparticles were obtained by coprecipitation of Fe^{2+} and Fe^{3+} salts in an alkaline medium. Then, the magnetite Fe_3O_4 was oxidized in maghemite Fe_2O_3 using nitrate acid containing iron nitrate. The nanoparticles were stabilized in distilled water using sodium citrate. The nanoparticles in the final solution are negatively charged. After the stabilization of the particles with sodium citrate, the pH is ≈7. These particles were stable between pH 3 and 9 The final solution contained 94 mg/mL of magnetic nanoparticles in the ferrofluid.

For the synthesis of Rhodamine B coated Fe_2O_3 nanoparticles in distilled water, a protocol previously reported by Bertorelle et al.[29] was followed. Briefly, the synthesis was based on the coupling of modified Rhodamine B molecules with dimercaptosuccinic acid onto positively charged γFe_2O_3 particles. Cystamine-modified Rhodamine B was coupled to DMSA-modified nanoparticles by stirring. The cystamine was used to couple 2 Rhodamine B molecules through amide bond formation. Then, Rhodamine B was bound to the nanoparticles via DMSA, which was complexed to the nanoparticle via carboxylic acid groups. The nanoparticles were then stabilized by pH adjustment in two steps (pH 9 and 7) with Tetramethylammonium hydroxide and HCl, respectively. Free Rhodamine B was removed by washing the nanoparticles with NaCl precipitation steps. The final dispersion was performed in distilled water.

Cell Culture and Harvesting for 3D Extrusion Printing: C2C12 mouse myoblasts were purchased from the American Type Culture Collection (ATCC, CRL-1772). Myoblasts were cultured in T-175 flasks (at 37 °C, 5% CO2) with Growth Media (GM) consisting of high glucose Dulbecco's modified Eagle's medium (DMEM; Gibco, 11 965 084) supplemented with 10% fetal bovine serum (Gibco), 200 nM l-glutamine (Gibco), and 1% penicillin-streptomycin (Gibco). Cells were harvested at 70–80% confluency with Trypsin (Gibco) and mixed at a concentration of 5×10^6 cells mL^{-1} with the bioink at 37 °C.

Bioink Preparation: The bioink was composed of a hydrogel mixture based on 7% w/v gelatin from porcine skin (Sigma, G2500), 4% w/v of fibrinogen from bovine plasma (Sigma, F8630), 5×10^6 C2C12 myoblasts per mL, and ferrofluid at different concentrations. To fabricate 1 ml of bioink, 70 mg of gelatin (Sigma-Aldrich) were dissolved in previously warmed GM supplemented with 1 mg ml^{-1} 6-aminocaproic acid (ACA, Sigma-Aldrich).The volume of GM/ACA varied depending on the ferrofluid concentration, for instance, to prepare 1%, 2.5%, and 5% (v/v) of ferrogel solutions, gelatin was dissolved in 490, 475, and 450 µl of GM/ACA, respectively. This solution was stirred at 40 °C until dissolved. In parallel, 40 mg of fibrinogen (Sigma-Aldrich) were dissolved in 0.5 mL of cold PBS 1X. Once both solutions were completely dissolved, they were mixed and left stirring at 37 °C. Then, the ferrofluid was added to the gelatin–fibrinogen mixture, that is, 10, 25, and 50 µl of the stock solution of ferrofluid were added to obtain the final hydrogels at 1%, 2.5%, and 5% of ferrofluid, respectively. C2C12 cells were recollected from the T-175 flasks with Trypsin and mixed with the bioink. The final cell-laden bioink was left at 5 °C for 5 min before printing.

3D Extrusion Printing: The two-post systems were printed with PDMS by extrusion of 1:20 ratio Sylgard PDMS. The 3D design of the shape of the infinity sign "∞" was exported as.stl file from Autocad, sliced and converted into a g-code in slic3r (version 1.6). This design was then fed into the Inkredible+ printer (Cellink) for extrusion printing. For 3D bioprinting of the ferromuscle, the bioink was first loaded into a syringe, kept at 5 °C for 5 min to induce gelatin gelation and then extruded through a 0.008 in conical plastic nozzle (Nordson). Although temperature control was not applied during the extrusion process, the bioink—pre-cooled to 5 °C—maintained consistent viscosity throughout the entire printing process which only took a few seconds per structure. The printed cell structures were immersed in a solution of thrombin (5 U mL^{-1}) for 10 min to cross-link the fibrinogen of the bioink. The printed tissues were maintained in GM supplemented with 1 mg ml^{-1} 6-aminocaproic acid (ACA, Sigma-Aldrich), to avoid degradation of collagen and fibrinogen by cell proteases, for 2 days. Then, cells were switched to differentiation media with ACA 1 mg ml^{-1} (DM/ACA) consisting of DMEM supplemented with 10% horse serum (Gibco), 200 nM l-glutamine, 1% penicillin-streptomycin and 50 ng ml^{-1} IGF-1 (Sigma-Aldrich), for at least 7 days, replacing with fresh DM/ACA every 2 days

Size Characterization of the Citrated Maghemite Nanoparticles with Transmission Electron Microscopy (TEM): Transmission electron microscopy (TEM) was employed to assess the morphology and size distribution of nanoparticles in a similar procedure as reported in literature.[37,38] The specific instrument employed for this analysis was the JEOL JEM-2800, operating at an acceleration voltage of 200 kV. To prepare TEM samples, the nanoparticle stock dispersion was diluted with water at an approximate ratio of 1:1000. Subsequently, a droplet of the diluted mixture was pipetted onto a TEM grid featuring a holey carbon film (Agar Scientific S147-4). The grid was then left to undergo evaporation, resulting in the deposition of the nanoparticles on the carbon film.

Through analysis of individual TEM images (Figure S3a, Supporting Information), the distribution of nanoparticle sizes (Figure S3b, Supporting Information) was determined by measuring the diameter of each particle using image processing tool Image J-Fiji (version 1.53t). The diameters of the nanoparticles were further subjected to a log-normal distribution fitting a log-normal equation $y = \frac{A}{xS\sqrt{2\pi}}\ exp\ (-\frac{(ln\ (x)-M)^2)}{2S^2})$, for $x > 0$, yielding $M = 2.2$, and $S = 0.35$. Consequently, the calculated average size of the nanoparticles was determined to be $\mu = e^{M+S^2/2} = 10.3$ nm, accompanied by a corresponding standard deviation of $\sigma = \sqrt{e^{2M+S^2}\,(e^{S^2}-1)} = 3.8$nm.

Rheology of the Bioinks: The rheological measurements of the magnetic bioinks containing ferrofluids at different concentrations (1%, 2.5%, and 5%) were conducted using the MCR 702 rheometer from Anton Paar, coupled with a CP40-1 cone plate, with a diameter of 40 mm (no. 2627). The cone plate maintained a fixed working gap of 0.078 mm. Each measurement was performed on 350 µl of samples, and the entire process was replicated three times to ensure accuracy. The average values were taken from these replicates. To determine the flow curves and viscosity values, a logarithmic shear rate ramp was employed, covering a range of values between 0.1 and 100 s^{-1}. Throughout the measurements, a constant temperature of 5 °C ± 0.2 °C was carefully maintained. This controlled temperature environment ensures consistency and reliability in the obtained rheological data.

Printability of the Ferrofluid-Based Bioink: Printability of the magnetic bioink was evaluated by measuring the width and height of infinity-shaped 3D-printed constructs with 1, 2, or 3 layers, using a printing pressure of 70 kPa. These constructs were made from a bioink formulation containing 2.5% ferrofluid, 7% gelatin, and 4% fibrinogen. Top-view images were taken with a bright-field microscope (Leica Thunder) while side-view images were obtained with a Thorlabs camera. Image analysis was performed using ImageJ software.

Confocal Imaging of Ferromuscles: Ferromuscles at day 7 of differentiation were washed three times with PBS 1X before fixation with 4% PFA for 30 min at room temperature. Then, after PBS washings, the tissues were imaged and recorded by confocal microscopy (LSM 710, 20×/1.0 water immersion objective, $\lambda_{ex} = 561$ nm and $\lambda_{em} = 563$–735 nm for Rhodamine B. The resolution of the acquired images was 1024 × 1024 pixels and the vertical interval Δz between two successive images was 2 µm. Images and 3D projections were exported from the instrument software (Zeiss Zen Black) in CZI and AVI formats, respectively, and further processed with Fiji (version 1.53t) for obtaining 3D visualization (Video S4, Supporting Information) and images in Figure 1F and Figure S2 (Supporting Information).

Magnetic Characterization of Muscle and Ferromuscle Tissues: Muscle tissues with and without ferrofluid were fixed with 4% PFA, washed with PBS and maintained in PBS with 50 mM sodium azide. The samples were picked from the PBS buffer and placed on a clean tissue for extracting the buffer solution. The dried fixed muscle tissues were consequently encapsulated in sample cups. Prior to and after the encapsulation the mass of each cap was measured with a Precision Balance (Pioneer PX 225D, Ohaus) and subtracted to obtain the mass of each fixed muscle tissue.

The mass of the fixed muscle tissue without ferrofluid was 2.27 mg and the mass of the muscle tissue with ferrofluid was 1.24 mg. The magnetic properties of both samples were measured within a Physical Property Measurement System (PPMS, QuantumDesign) using the vibrating sample magnetometer (VSM) mode. The vibrating samples were excited with a magnetic field strength in a range from -1 to 1 [T] and the magnetic moment [emu] was measured. The density of the muscle tissues was assumed to be 1060 kg m^{-3} following[39] to obtain the volume magnetization of the samples shown in Figure S1 (Supporting Information).

Degradation of the Ferromuscle Tissue: After full differentiation of the control tissues and ferromuscles (containing 2.5% of ferrofluid) at day 9, the samples were cultured for 21 days more in differentiation media with or without protease inhibitor (ACA). Cell media was replaced every two days. Images of the muscle tissues were taken at different time points (day 0, 14, and 21) using bright-field microscopy. The measurements of the areas were performed using Image J software.

Cell Viability Tests: Viability of ferromuscles and control muscles was performed at day 3 and 6 of culture using the LIVE/DEAD™ Viability/Cytotoxicity Kit, for mammalian cells (Invitrogen, L3224) following the protocol indicated by the company. The cell nuclei were stained by adding Hoechst 33 342 (0.5 µL mL^{-1}; Invitrogen, H1399) to the Live/Dead staining solution, and incubating the samples for 30 min at 37 °C.

Immunostaining of 3D Bioprinted Skeletal Muscle Tissues: Control and ferromuscle tissues (with 2.5% of ferrofluid) were washed three times with PBS and fixed with a 3.7% (v/v) paraformaldehyde solution in PBS for 60 min at room temperature. Following fixation, the samples were washed three times with PBS before cell permeabilization using 0.3% (v/v) Triton-X-100 in PBS. After two additional PBS washes, non-specific binding was blocked by incubating the constructs in 5% (w/v) Bovine Serum Albumin (BSA) in PBS. Samples were then incubated overnight at 4 °C with the primary already conjugated antibody Alexa Fluor 488-conjugated Anti-Myosin 4, also known as Myosin Heavy Chain II-b, (eBioscience, 53-6503-82, 1:100 dilution), under dark conditions in 5% BSA. After this incubation period, excess antibody was removed by PBS washes, and F-actin was stained using ReadyProbes 555 (Invitrogen, R37112) for 2 h at room temperature in the dark, following the manufacturer's protocol. Unbound antibodies were then washed away with PBS, and a PBS solution containing Hoechst 33 342 (1 µL mL^{-1}, Life Technologies) was added for 10 min at room temperature to stain cell nuclei. Finally, the samples were washed again twice with PBS and were stored at 4 °C until further analysis. Imaging was performed using a Leica Thunder microscope and a Zeiss LSM 800 confocal scanning laser microscope (CSLM), with excitation lasers at 488, 555, and 405 nm for Myosin 4, F-actin, and nuclei, respectively. The orientation and alignment of myotubes were analyzed using ImageJ with plugin directionality. Angle dispersion values were obtained from the Fast Fourier Transform (FFT) of the Myosin 4 immunostaining images from control and Ferromuscles at day 9.

Force Measurements: Electrical pulse stimulation with a 2 ms pulse width and a 15 V amplitude was applied at a frequency of 1 Hz using custom-made graphite-based electrodes placed in the Petri dish containing the muscle tissue in DM/ACA, and connected to the electrical stimulation setup, consisting of an oscilloscope, a waveform generator, and a power supply. The deflection of the PDMS posts was recorded via bright-field microscopy.

Euler-Bernoullis beam bending equation was used to calculate the forces exerted against the posts, taking into account the stiffness of the posts (206 kPa), as previously reported.[25] Motion analysis was performed with a lab-made python tracking script[40] that recognizes the region of interest indicated by the user, and tracks this object throughout the video.

Sample Cryosection and Immunofluorescence Staining: Muscle tissues were washed three times with PBS 1X before fixation with 4% PFA for 30 min at room temperature. Fixed samples were washed again in PBS 1X and then embedded in Optimal Cutting Temperature compound (OCT, Sigma-Aldrich – P0091-6×120ML) within a disposable plastic cryomold. For cryopreserving the samples, the cryomolds were immersed in isopentane, which was previously cooled in liquid Nitrogen, until the OCT was clearly frozen showing a whiteish color. Samples were stored at -20 °C until sectioning, which was done with a cryostat (Leica CM1900), obtaining sections of 20 µm thickness that were placed on Superfrost PlusTM Adhesion slides and stored at -20 °C. To perform the immunofluorescence staining muscle cryosections (cross sections) were first encircled with a PAP pen to avoid the leakage of the staining solutions through the slides. Samples were permeabilized for 10 min with a PBS-T solution containing PBS 1X and 0.1% Triton-X100, then blocked for 30 min at room temperature with a blocking buffer containing 0.3% Triton-X100 and 3% BSA in PBS 1X. To identify the formation of aligned myotubes, samples were incubated with Myosin 4 Monoclonal Antibody (MHCIIb) conjugated with Alexa Fluor 488 (Invitrogen, 53-6503-82) at a 1/400 ratio in blocker buffer, overnight at 4 °C and dark conditions. Then, cross sections were washed with PBS-T three times before incubating with 2 µm ml^{-1} solution of Hoechst 33 342 in PBS 1X for nucleus staining. Samples were washed again with PBS 1X and mounting media (Invitrogen ProLong Diamond Antifade Mountant, P36961) was added. Finally, a coverslip was placed on top of the stained cryosections, and nail polish was used to seal the edges. Samples were stored at 4 °C until imaging. The penetration of ferrofluid was quantified and displayed by the corrected total cell fluorescence (CTFC = Integrated fluorescence intensity – (Area x mean fluorescent of background). Values of area and integrated fluorescence intensity were obtained using Image J. The quantification of percentage of MyHCIIb-positive cells was performed using the plugin Cell Counter from Image J.

RNA Extraction and Real Time Quantitative PCR (RT-qPCR): To assess the mRNA expression of myogenic markers, including MyoD, myogenin, MyHCI, MyHCIIa, and MyHCIIb, total RNA was extracted from three biological replicates of control and ferromuscle tissues at days 0, 4, and 9 of differentiation. Please note that day 0 (D0) of differentiation refers to the day when the growth media was switched to differentiation media, which occurred two days after the 3D bioprinting of the tissues. RNA isolation was performed using the RNeasy Mini Kit (Qiagen, 74 134), and its concentration was determined by measuring absorbance at 260 nm with a NanoDrop spectrophotometer (ND-1000, NanoDrop). Complementary DNA (cDNA) synthesis was carried out using the RevertAid First Strand cDNA Synthesis Kit (Thermo Scientific, K1622). Subsequently, 500 ng of cDNA was combined with gene-specific forward and reverse primers and PowerUp SYBR Green Master Mix (Applied Biosystems, A25742), following the manufacturer's protocol. RT-qPCR was conducted using an Applied Biosystems StepOnePlus Real-Time PCR system (Applied Biosystems, 4 376 600). The primer sequences used in this study are provided in Supporting Information. Gene expression levels were normalized to GAPDH.

Statistical Analysis: Two-way analysis of variance (ANOVA) followed by a Tukey's multiple comparisons test was performed in GraphPad Prism to evaluate the significance ($p < 0.05$) on values from fiber width and height of the 3D printed constructs. Analysis of variance for the viability tests was performed in OriginPro (version 1.6) with a one-way ANOVA, Bonferroni method with a significance threshold of 0.05, see Table S1 (Supporting Information). Statistical analysis of force measurements was performed with a one-way ANOVA ($p < 0.05$) using GraphPad Prism.

Supporting Information

Supporting Information is available from the Wiley Online Library or from the author.

Acknowledgements

Z.M.C. acknowledges the funding support by the Academy of Finland under Grant 342268. V.M. thanks the La Caixa Foundation for funding support. J.F., S.L., G.C., P.C. and S.S. acknowledges the financial support from the European Union's Horizon Europe research and innovation programme under grant agreement No. 101070328 (Biomeld). M.G. acknowledges the financial support from the Spanish Ministry of Science through the Ramon y Cajal Grant No. RYC2020-945030119-I, and "Unidad Maria de Maetzu" funded by Agencia Estatal de Investigación (2021

CEX2021-001202-M). S.S., M.G. and J.F. acknowledges CERCA program by the Generalitat de Catalunya, the Secretaria d'Universitats i Recerca del Departament d'Empresa i Coneixement de la Generalitat de Catalunya through the project 2021 SGR 01606, and the "Centro de Excelencia Severo Ochoa", funded by Agencia Estatal de Investigación (CEX2018-000789-S).

Conflict of Interest

The authors declare no conflict of interest.

Data Availability Statement

The data that support the findings of this study are available from the corresponding author upon reasonable request.

Keywords

3D printing, ferrofluid, magnetic bioink, muscle actuators, muscle tissue

Received: November 1, 2024
Revised: April 7, 2025
Published online: June 25, 2025

[1] J. Groll, T. Boland, T. Blunk, J. A. Burdick, D.-W. Cho, P. D. Dalton, B. Derby, G. Forgacs, Q. Li, V. A. Mironov, L. Moroni, M. Nakamura, W. Shu, S. Takeuchi, G. Vozzi, T. B. F. Woodfield, T. Xu, J. J. Yoo, J. Malda, *Biofabrication* **2016**, *8*, 013001.
[2] S. V. Murphy, A. Atala, *Nat. Biotechnol.* **2014**, *32*, 773.
[3] M. Samandari, J. Quint, A. Rodríguez-delaRosa, I. Sinha, O. Pourquié, A. Tamayol, *Adv. Mater.* **2022**, *34*, 2105883.
[4] G. Decante, J. B. Costa, J. Silva-Correia, M. N. Collins, R. L. Reis, J. M. Oliveira, *Biofabrication* **2021**, *13*, 032001.
[5] B. S. Kim, S. Das, J. Jang, D.-W. Cho, *Chem. Rev.* **2020**, *120*, 10608.
[6] E. Bianchi, B. Vigani, C. Viseras, F. Ferrari, S. Rossi, G. Sandri, *Pharmaceutics* **2022**, *14*, 1127.
[7] B. G. Molina, J. Fuentes, C. Alemán, S. Sánchez, *Biosens. Bioelectron.* **2024**, *251*, 116117.
[8] M. Filippi, F. Garello, O. Yasa, J. Kasamkattil, A. Scherberich, R. K. Katzschmann, *Small* **2022**, *18*, 2104079.
[9] N. R. de Barros, M. A. Darabi, X. Ma, S. E. Diltemiz, M. Ermis, A. Hassani Najafabadi, S. Nadine, E. A. Banton, K. Mandal, R. Abbasgholizadeh, N. Falcone, J. F. Mano, R. Nasiri, R. D. Herculano, Y. Zhu, S. Ostrovidov, J. Lee, H. Kim, V. Hosseini, M. R. Dokmeci, S. Ahadian, A. Khademhosseini, *Macromol. Biosci.* **2023**, *23*, 2300276.
[10] A. Pardo, M. Gómez-Florit, S. Barbosa, P. Taboada, R. M. A. Domingues, M. E. Gomes, *ACS Nano* **2021**, *15*, 175.
[11] A. Van de Walle, J. E. Perez, A. Abou-Hassan, M. Hémadi, N. Luciani, C. Wilhelm, *Mater. Today Nano* **2020**, *11*, 100084.
[12] Y. Huang, J. C. Hsu, H. Koo, D. P. Cormode, *Theranostics* **2022**, *12*, 796.
[13] M. Shi, L. Bai, M. Xu, R. Dong, Z. Yin, W. Zhao, B. Guo, J. Hu, *Chem. Eng. J.* **2024**, *484*, 149019.
[14] G. Cedillo-Servin, O. Dahri, J. Meneses, J. van Duijn, H. Moon, F. Sage, J. Silva, A. Pereira, F. D. Magalhães, J. Malda, N. Geijsen, A. M. Pinto, M. Castilho, *Small* **2024**, *20*, 2307178.
[15] E. Ergene, G. Liman, P. Yilgor, G. Demirel, *Adv. Mater. Technol.* **2024**, *9*, 2400119.
[16] E. S. Ko, C. Kim, Y. Choi, K. Y. Lee, *Carbohydr. Polym.* **2020**, *245*, 116496.
[17] Y. Choi, C. Kim, H. S. Kim, C. Moon, K. Y. Lee, *Colloids Surf., B Biointerfaces* **2021**, *208*, 112108.
[18] C. A. Cezar, S. M. Kennedy, M. Mehta, J. C. Weaver, L. Gu, H. Vandenburgh, D. J. Mooney, *Adv. Healthcare Mater.* **2014**, *3*, 1869.
[19] C. A. Cezar, D. J. Mooney, *Adv. Drug Delivery Rev.* **2015**, *84*, 188.
[20] C. A. Cezar, E. T. Roche, H. H. Vandenburgh, G. N. Duda, C. J. Walsh, D. J. Mooney, *Proc. Natl. Acad. Sci. USA* **2016**, *113*, 1534.
[21] P. Zhuang, J. An, C. K. Chua, L. P. Tan, *Mater. Des.* **2020**, *193*, 108794.
[22] C. Cvetkovic, M. C. Ferrall-Fairbanks, E. Ko, L. Grant, H. Kong, M. O. Platt, R. Bashir, *Sci. Rep.* **2017**, *7*, 3775.
[23] R. Andreazza, A. Morales, S. Pieniz, J. Labidi, *Polymers (Basel)* **2023**, *15*, 1026.
[24] Y. Wei, L. Quan, C. Zhou, Q. Zhan, *Nanomedicine* **2018**, *13*, 1495.
[25] R. Mestre, T. Patiño, X. Barceló, S. Anand, A. Pérez-Jiménez, S. Sánchez, *Adv. Mater. Technol.* **2019**, *4*, 1800631.
[26] X. Hu, W. Liu, L. Sun, S. Xu, T. Wang, J. Meng, T. Wen, Q. Liu, J. Liu, H. Xu, *Int. J. Mol. Sci.* **2022**, *23*, 4440.
[27] L. Zhou, Y. Xi, Y. Xue, M. Wang, Y. Liu, Y. Guo, B. Lei, *Adv. Funct. Mater.* **2019**, *29*, 1806883.
[28] R. Mestre, J. Fuentes, L. Lefaix, J. Wang, M. Guix, G. Murillo, R. Bashir, S. Sánchez, *Adv. Mater. Technol.* **2023**, *8*, 2200505.
[29] A. Abdal Dayem, S. Bin Lee, S.-G. Cho, *Nanomaterials* **2018**, *8*, 761.
[30] A. Rossi, G. Bassi, C. Cunha, C. Baldisserri, N. Ravaglia, D. Gardini, F. Molinari, F. Lista, F. J. Teran, A. Piperno, M. Montesi, S. Panseri, *J. Colloid Interface Sci.* **2025**, *678*, 334.
[31] M. Guix, R. Mestre, T. Patiño, M. De Corato, J. Fuentes, G. Zarpellon, S. Sánchez, *Sci. Rob.* **2021**, *6*, abe7577.
[32] G. J. Pagan-Diaz, X. Zhang, L. Grant, Y. Kim, O. Aydin, C. Cvetkovic, E. Ko, E. Solomon, J. Hollis, H. Kong, T. Saif, M. Gazzola, R. Bashir, *Adv. Funct. Mater.* **2018**, *28*, 1870159.
[33] J. Malda, J. Visser, F. P. Melchels, T. Jüngst, W. E. Hennink, W. J. A. Dhert, J. Groll, D. W. Hutmacher, *Adv. Mater.* **2013**, *25*, 5011.
[34] C. Villa, V. Secchi, M. Macchi, L. Tripodi, E. Trombetta, D. Zambroni, F. Padelli, M. Mauri, M. Molinaro, R. Oddone, A. Farini, A. De Palma, L. Varela Pinzon, F. Santarelli, R. Simonutti, P. Mauri, L. Porretti, M. Campione, D. Aquino, A. Monguzzi, Y. Torrente, *Nat. Nanotechnol.* **2024**, *19*, 1532.
[35] N. Rose, B. Estrada Chavez, S. Sonam, T. Nguyen, G. Grenci, A. Bigot, A. Muchir, B. Ladoux, B. Cadot, F. Le Grand, L. Trichet, *Biomaterials* **2023**, *293*, 121935.
[36] Y. Kim, Y. Yang, X. Zhang, Z. Li, A. Vázquez-Guardado, I. Park, J. Wang, A. I. Efimov, Z. Dou, Y. Wang, J. Park, H. Luan, X. Ni, Y. S. Kim, J. Baek, J. J. Park, Z. Xie, H. Zhao, M. Gazzola, J. A. Rogers, R. Bashir, *Sci. Rob.* **2023**, *8*, add1053.
[37] R. Massart, *IEEE Trans. Magn.* **1981**, *17*, 1247.
[38] C. Rigoni, G. Beaune, B. Harnist, F. Sohrabi, J. V. I. Timonen, *Commun. Mater.* **2022**, *3*, 26.
[39] K. C. Leonard, N. Worden, M. L. Boettcher, E. Dickinson, K. M. Omstead, A. M. Burrows, A. Hartstone-Rose, *Sci. Rep.* **2021**, *11*, 2114.
[40] R. Mestre, NMTT: Nano-micromotor tracking tool, https://doi.org/10.5281/zenodo.5905482 (accessed: June 2022).